JWST detection of a carbon dioxide dominated gas coma surrounding interstellar object 3I/ATLAS

Martin A. Cordiner,^{1,2} Nathan X. Roth,^{1,3} Michael S. P. Kelley,⁴ Dennis Bodewits,⁵ Steven B. Charnley,¹ Maria N. Drozdovskaya,⁶ Davide Farnocchia,⁷ Marco Micheli,⁸ Stefanie N. Milam,¹ Cyrielle Opitom,⁹ Megan E. Schwamb,¹⁰ Cristina A. Thomas,¹¹ and Stefano Bagnulo¹²

¹ Astrochemistry Laboratory, NASA Goddard Space Flight Center, 8800 Greenbelt Road, Greenbelt, MD 20771, USA.

² Department of Physics, Catholic University of America, Washington, DC 20064, USA.

³Department of Physics, American University, 4400 Massachusetts Avenue, NW, Washington, DC 20016, USA.

⁴Department of Astronomy, University of Maryland, College Park, MD 20742-0001, USA.

⁵ Physics Department, Edmund C. Leach Science Center, Auburn University, Auburn, AL 36849, USA.

⁶ Physikalisch-Meteorologisches Observatorium Davos und Weltstrahlungszentrum (PMOD/WRC), Dorfstrasse 33, CH-7260, Davos Dorf, Switzerland.

⁷ Jet Propulsion Laboratory, California Institute of Technology, 4800 Oak Grove Dr., Pasadena, CA 91109, USA.

⁸ ESA NEO Coordination Centre, Planetary Defence Office, European Space Agency, Largo Galileo Galileo, 1, 00044 Frascati (RM), Italy.
⁹ Institute for Astronomy, University of Edinburgh, Royal Observatory, Edinburgh EH9 3HJ, UK.

Astrophysics Research Centre, School of Mathematics and Physics, Queen's University Belfast, Belfast BT7 1NN, UK.
 Northern Arizona University, Department of Astronomy and Planetary Science, P.O. Box 6010, Flagstaff, AZ, 86011 USA.
 Armagh Observatory and Planetarium, College Hill, Armagh, BT61 9DG, UK.

ABSTRACT

3I/ATLAS is the third confirmed interstellar object to visit our Solar System, and only the second to display a clear coma. Infrared spectroscopy with the James Webb Space Telescope (JWST) provides the opportunity to measure its coma composition and determine the primary activity drivers. We report the first results from our JWST NIRSpec campaign for 3I/ATLAS, at an inbound heliocentric distance of $r_H=3.32$ au. The spectral images (spanning 0.6– $5.3~\mu m$) reveal a CO₂ dominated coma, with enhanced outgassing in the sunward direction, and the presence of H₂O, CO, water ice, dust and a tentative detection of OCS. The coma CO₂/H₂O mixing ratio of 7.6 ± 0.3 is among the highest ever observed in a comet, and is 4.5σ above the trend as a function of r_H for long-period and Jupiter-family comets (excluding the outlier C/2016 R2). Our observations are compatible with an intrinsically CO₂-rich nucleus, which may indicate that 3I/ATLAS contains ices exposed to higher levels of radiation than Solar System comets, or that it formed close to the CO₂ ice line in its parent protoplanetary disk. A low coma H₂O gas abundance may also be implied, for example, due to inhibited heat penetration into the nucleus, which could suppress the H₂O sublimation rate relative to CO₂ and CO.

Keywords: Comets, individual: 3I/ATLAS — Techniques: Imaging Spectroscopy — Techniques: Infrared — Molecular lines — Astrochemistry

1. INTRODUCTION

Comets and planetesimals are theorized to form in large numbers during the accretion of planetary systems. Many of these small bodies, composed of ice, rock, and dust, are subsequently expected to be ejected into interstellar space through gravitational encounters with larger, planetary or stellar, bodies (L. Dones et al. 2004; H. F. Levison et al. 2010; S. N. Raymond et al.

Corresponding author: M. A. Cordiner martin.cordiner@nasa.gov

2018; S. Pfalzner & K. Vincke 2020; X.-L. Zheng & J.-L. Zhou 2025). The apparitions of the first confirmed interstellar objects (ISOs) 1I/'Oumuamua in October 2017 and 2I/Borisov in August 2019 provided confirmation of this theory, and offered an unprecedented opportunity to study the nature of matter delivered to our Solar System from a distant planetary system, thus spawning a new field of planetary science.

Due to its faintness and short observing window, spectroscopic characterization of volatiles from 1I/'Oumuamua proved elusive, so the composition of this object remains highly uncertain ('Oumuamua ISSI

2 Cordiner et al.

Team et al. 2019). On the other hand, for the intrinsically brighter and more active 2I/Borisov, ultraviolet, optical, and submillimeter observations (e.g. M. A. Cordiner et al. 2020; D. Bodewits et al. 2020; P. Guzik & M. Drahus 2021; C. Opitom et al. 2021; Z. Xing et al. 2020) provided intriguing glimpses of its coma composition, and revealed an object that was similar in many ways to the well-studied comets from our own Solar System, but with an unusually strong enrichment in carbon monoxide (CO) (M. A. Cordiner et al. 2020; D. Bodewits et al. 2020). Considering the difficulty of studying the ices in the midplanes of protoplanetary disks and planetary systems elsewhere in our Galaxy, continued spectroscopic observations of interstellar objects have the potential to reveal crucial details on the physics and chemistry of planet formation in planetary systems other than our own.

The discovery of a third interstellar object (3I/ATLAS) was announced on 2025 July 1 by the Asteroid Terrestrial-impact Last Alert System (ATLAS; J. L. Tonry et al. 2018). Based on its inbound orbital eccentricity (6.144 \pm 0.016) and heliocentric radial velocity projected to infinity $(57.95 \pm 0.05 \text{ km s}^{-1})$ (D. Z. Seligman et al. 2025), 3I/ATLAS has been confirmed to be on a gravitationally unbound, hyperbolic interstellar trajectory. Dynamical modeling of a population of Galactic interstellar objects (ISOs) shows that the high velocity of 3I/ATLAS is consistent with a relatively large dynamical age of 3–11 billion years (M. J. Hopkins et al. 2025; A. G. Taylor & D. Z. Seligman 2025). This age, coupled with its trajectory, implies 3I/ATLAS could have originated from a relatively old, low-metallicity stellar system, plausibly from the kinematically hot, "thick disk" population of the Milky Way. Chemical differences between the volatile content of 3I/ATLAS and our Solar System's comets may therefore be expected.

Similar to 2I/Borisov, 3I/ATLAS has been shown to display clear cometary activity (D. Jewitt & J. Luu 2025; M. R. Alarcon et al. 2025; M. Minev et al. 2025). Early spectroscopic and photometric observations revealed a compact nucleus (effective radius < 2.8 km), a bright, dusty coma, with a dust mass-loss rate of 12–120 kg s⁻¹ (D. Jewitt et al. 2025), and a red spectral slope, with possible water ice absorption at 2.0 μ m (T. Kareta et al. in press; B. Yang et al. 2025). The Neil Gehrels-Swift Observatory detected ultraviolet emission from the gasphase OH radical (Z. Xing et al. 2025), and assuming H₂O to be the photolysis parent, a water production rate of $(1.36 \pm 0.35) \times 10^{27}$ s⁻¹ was derived at a heliocentric distance of $r_H = 2.9$ au.

Here, we present the first set of infrared spectroscopic observations from our campaign to observe 3I/ATLAS using the James Webb Space Telescope (JWST). This article focuses on analyzing the rovibrational fluorescence emission from H₂O, CO₂, and CO, which are the main drivers of coma activity in typical Solar System comets. Molecular production rates and mixing ratios are derived, enabling chemical characterization of the object's volatile gas inventory.

2. OBSERVATIONS

Observations of 3I/ATLAS were performed using JWST (J. P. Gardner et al. 2023) on UT 2025-08-06 between 11:02–11:20, using the NIRSpec integral field unit (IFU; T. Böker et al. 2022), as part of program ID 5094. The PRISM dispersive element was used, resulting in a 30 × 30 array of spectra covering $\lambda = 0.6$ –5.3 μ m, with a resolving power $R_{\lambda} = \lambda/\Delta\lambda$ that varies from \approx 30 at 1.2 μ m to \approx 300 at 5.3 μ m. The IFU pixel size is 0".1, which is approximately the same as the FWHM of the JWST point-spread function at 3 μ m.

3I/ATLAS was acquired and tracked in the IFU using JPL Horizons ephemeris solution #19, when the object was 2.73 au from the telescope, at $r_H = 3.32$ au and a phase angle of 16.1°. The total on-target exposure duration was 640 s, divided across four dither positions, each spatially separated (in the approximate shape of a square) with offsets of ~ 0.2 from the (central) targeted position. The data were reduced using the JWST Calibration Pipeline software version v1.19.1 (H. Bushouse et al. 2025) using the JWST Calibration Reference Data System context file 1413. The four dithers were shifted and combined in the rest frame of the comet during image processing, thus allowing detector artifacts and cosmic rays to be identified and removed. A similar set of four exposures of the sky background was obtained, offset by 180" along the horizontal axis of the IFU aperture. This allows contamination from background infrared sources, zodiacal light, and the telescope to be identified and subtracted. Data cubes with and without background subtraction were produced. The latter allows for the analysis of faint gas emission bands without the contribution of additional noise from a background subtraction. For each spectral data cube, the pipeline produces uncertainty and data quality maps, which were used during our analysis, in particular, for the derivation of formal (1σ) error estimates. After combining the four dithered observations, the absolute calibration accuracy is expected to be 3%.¹³

¹³ https://jwst-docs.stsci.edu/jwst-calibration-status/nirspeccalibration-status/nirspec-ifu-calibration-status

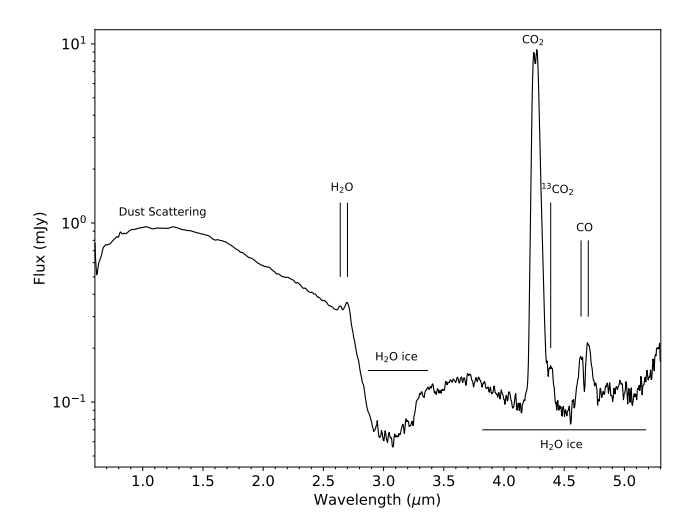


Figure 1. JWST spectrum of 3I/ATLAS using the NIRSpec PRISM (sky background subtracted), spatially integrated over the IFU field of view, and plotted with a logarithmic flux scale. Prominent spectral features are labeled.

3. RESULTS

The observed flux was integrated over the entire IFU field of view to produce the spectrum shown in Figure 1. Prominent features include a broad maximum at around 1.2 μ m, due to scattered sunlight from coma dust grains, and a strong, narrow (double) peak at 4.3 μ m, which is assigned to the main (ν_3) rovibrational emission band of gas-phase CO₂. Weaker gas emission bands from H₂O ($\nu_1+\nu_3$), CO (v=1-0) and ¹³CO₂ (ν_3) are also present, along with broad absorption features centered around 3.0 μ m and 4.5 μ m, attributed to the OH stretching mode and lattice vibrations, respectively, of H₂O ice in the coma — likely in the form of small (\lesssim 10 micronsized) icy grains (M. H. Moore & R. L. Hudson 1992; G. Leto & G. A. Baratta 2003; R. M. Mastrapa et al. 2009).

To isolate the CO₂, H₂O, and CO gas emission features, spectral data were extracted for each IFU pixel within the vicinity of each emission band, and a polynomial continuum fit was performed, excluding the spectral region directly inside each molecular emission band (see Section 4). For CO₂ and CO, a 3rd-order polynomial was used, whereas for H₂O a 5th-order polynomial was used, to better fit the wing of the 3.0 μm ice band . After continuum subtraction, the IFU spectra were integrated across the detected full emission width of each feature, then plotted as maps in Figure 2. The spatially averaged, continuum-subtracted emission band profile for each molecule is shown in the upper-right inset of their respective panels. The $\sim 1.2~\mu m$ scattered light image (integrated between 0.8–1.4 μm) is also shown. The

continuum brightness at 0.75 and 1.25 μ m is 101±3 and 124±4 μ Jy inside a 0″8-diameter circular aperture, corresponding to cometary $Af\rho$ quantities (M. F. A'Hearn et al. 1984) of 392 and 492 cm, respectively (quoted without a correction for phase darkening).

The gas and dust maps for 3I/ATLAS show a welldefined peak, offset East from the center of the IFU by 1"2 (Figure 2). As shown by a later ephemeris reconstruction, about 0".5 of the offset can be explained by a 1.7σ error on the predicted ephemeris, while the remaining 0".7 offset remains under investigation; the astrometry available to-date shows no evidence for nongravitational acceleration of 3I/ATLAS. The 1.2 μ m scattered light and CO₂ emission maps reveal an extended coma of dust and gas that spans the full extent of the NIRSpec IFU. The H₂O and CO emission is weaker, and therefore noisier, but nevertheless confirms the presence of a spatially extended molecular coma. While the scattered light shows a clear asymmetry along the Sun-comet axis — enhanced in the direction of the sky-projected comet-Sun and velocity vectors (see also D. Jewitt et al. 2025; C. O. Chandler et al. 2025) — the gas distributions (particularly CO₂ and CO), appear relatively more symmetrical.

To further investigate the coma structure, a $1/\rho$ enhanced version of the dust map (where ρ is the skyprojected nucleocentric distance), is shown in Figure 3, and similarly for the gas maps in Appendix A (Figure 7). In these enhanced maps, the dominant coma spatial feature: $\sim 1/\rho$ dilution of the observed column densities due to quasi-spherical expansion, has been divided out. The $1/\rho$ -enhanced 1.2 μ m map reveals a strong, plume-like feature emanating from the pseudo-nucleus in the approximate direction of the Sun (slightly north of west), with an additional, weaker feature to the northeast. Since the dust in relatively faint comets such as 3I/ATLAS is optically thin at this wavelength, the shape of this feature is interpreted as resulting from an enhanced coma dust density in the sunward direction, potentially from the fragmentation of dust grains increasing the scattering cross section with distance from the nucleus (M. R. Combi 1994; T. J. Jones et al. 2008). The gas maps on the other hand, show more subtle asymmetries. CO₂ exhibits an azimuthal minimum towards the north, that we attribute to a combination of weak coma sub-structure and optical depth effects, since CO₂ becomes optically thick close to the nucleus.

Taking the ratio of continuum-subtracted fluxes within a 0".4-radius circular aperture centered 0".6 from the brightest pixel on the sunward (S) and antisunward (S') sides, gives S/S' = 1.54 for the $(1.2 \ \mu\text{m})$ dust, 1.03 for CO_2 , 1.31 for H_2O and 1.00 for CO (with un-

4 Cordiner et al.

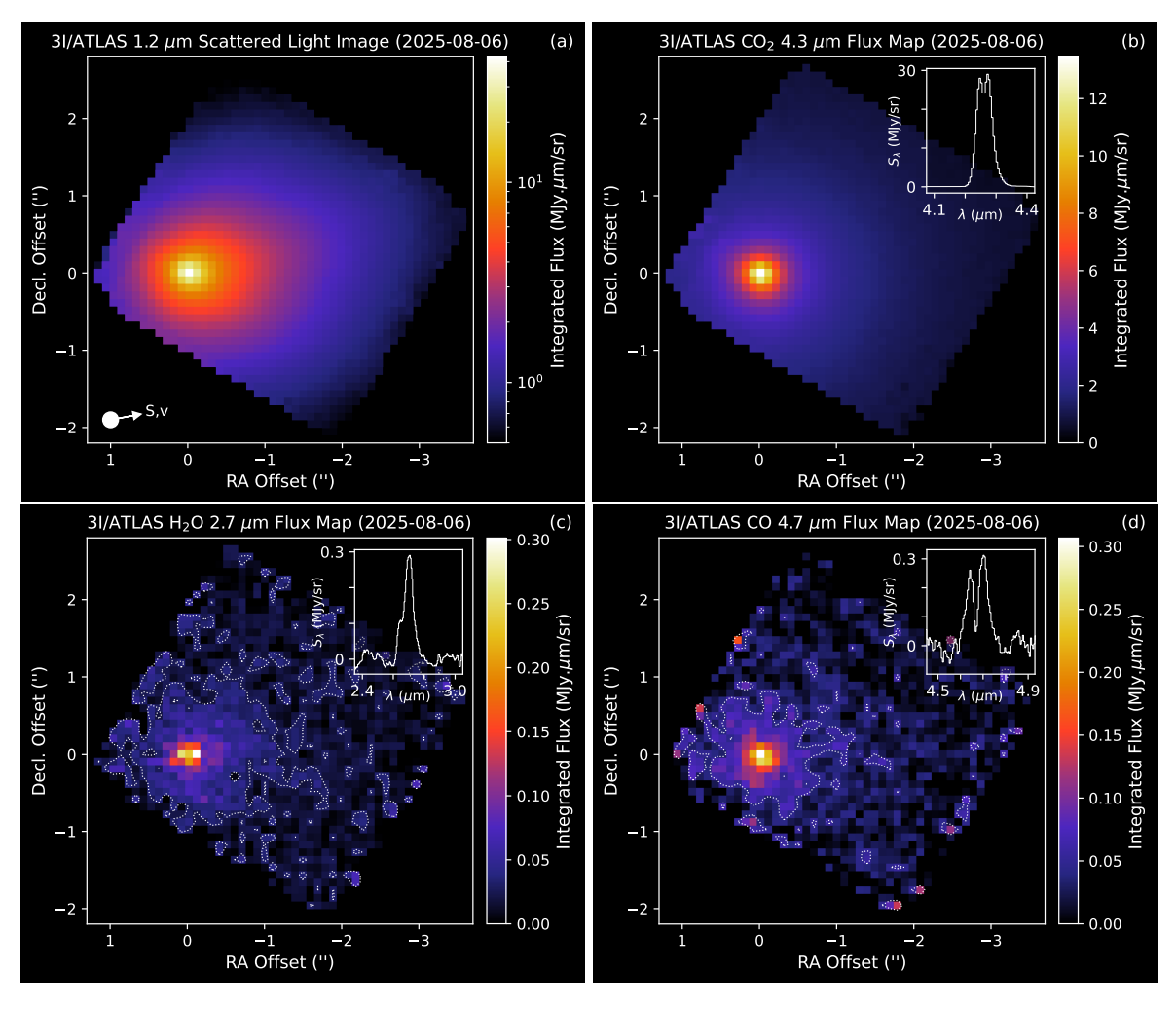


Figure 2. Spectrally integrated flux maps for 3I/ATLAS observed using JWST NIRSpec: (a) scattered light from coma dust at $\sim 1.2~\mu\text{m}$, plotted on a logarithmic scale to highlight the coma shape, (b) CO₂ at 4.3 μm , (c) H₂O at 2.7 μm , and (d) CO at 4.7 μm . Image axes are aligned with the equatorial (RA/decl.) grid. Molecular line emission has been isolated by subtracting a polynomial fit to the adjacent continuum. Spatial coordinates are with respect to the brightest pixel in the continuum dust map. For panels (b)–(d), inset plots (upper right) show the continuum-subtracted spectra, spatially averaged across all IFU pixels. Panel (a) lower left corner shows the direction of the (sky-projected) comet-sun (S) and nucleus velocity (v) vectors (which are too close to distinguish). For H₂O and CO, the 3 σ noise level is shown with a dotted contour; for the dust and CO₂ maps, the 3 σ noise level lies outside the IFU boundary, so is not shown.

certainties of < 1% on all measurements). Our observations thus reveal a heterogeneous coma morphology consistent with different outgassing patterns for the different species. Such heterogeneity can be explained by various factors, such as the different molecular sublimation temperatures, nucleus release and coma acceleration mechanisms, as well as differing inertial/fluid-dynamical properties for the gas and dust. The degree of asymmetry of the observed gases is likely related to their sublimation temperatures (T_{sub}) , with $S/S'(H_2O) > S/S'(CO_2) > S/S'(CO)$, congruent with $T_{sub}(H_2O) > T_{sub}(CO_2) > T_{sub}(CO)$ (M. Womack et al. 2017). This implies that the sublimation of CO_2 and CO is more fully activated than H_2O . Full interpretation of

the observed outgassing morphologies, including the surprisingly strong sunward dust enhancement, will require detailed physical modeling. Nevertheless, our data are consistent with the origin of this dust feature being influenced by enhanced gas sublimation (and therefore, outgassing) rates associated with the higher temperature on the dayside of the nucleus.

The 3.0 μ m H₂O ice band depth is 78.3 \pm 0.2% at 2.9–3.1 μ m, with respect to the continuum at 2.5 and 3.8 μ m. The band remains strong across the field of view, varying by no more than 10%. Water ice also has broad near-infrared absorption features at 1.5, 2.0, 3.0, and 4.5 μ m. The 4.5 μ m band is difficult to measure in our data due to blending with CO₂ and CO gas emission and likely

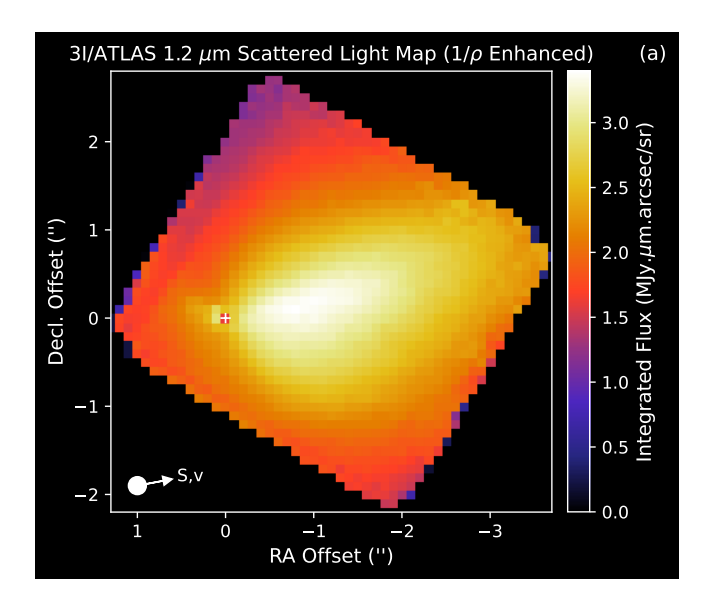


Figure 3. $1/\rho$ -enhanced 1.2 μ m scattered light map for 3I/ATLAS observed using JWST NIRSpec. This is panel (a) from Figure 2, multiplied by ρ (the sky-projected distance from the center of the brightest pixel — the assumed location of the nucleus). Similarly enhanced maps of the gas emission are shown in Appendix A (Figure 7). Image axes are aligned with the equatorial (RA/decl.) grid. The white cross shows the position of the nucleus pixel.

thermal continuum, the 2.0 μ m band appears very weak, and there is no discernible 1.5 μ m band. Furthermore, the 2.0 μ m spectral region in our combined IFU dataset is affected by several bad pixels. The average 2.0 μ m band depth in the two dither positions with clean spectra in this region is $(1.8\pm0.1)\%$. This was estimated by normalizing the reflectance spectrum within a 0".4 radius aperture with a linear fit between 1.75 and 2.22 μ m, and measuring the mean value at 1.95–2.05 μ m. The appearance of a strong 3- μ m band, but weak or absent 1.5- and 2.0- μ m bands implies the ice grains are micrometer size or smaller, while the shape of the band may be consistent with contributions from crystalline as well as amorphous ice (S. Protopapa et al. 2014).

4. SPECTRAL MODELING

To derive gas production rates (Q) and rotational temperatures (T_{rot}) , the background-subtracted IFU data for CO₂, CO, and H₂O were subject to spectral modeling using optimal estimation routines as part of the Planetary Spectrum Generator (PSG; G. L. Villanueva et al. 2018). Initially, we constructed spectral models by taking the average spectrum for each gas inside a $\rho = 0\%625$ (1240 km) circular aperture centered on the nucleus. The relatively high signal-to-noise ratio (SNR) in this IFU region assisted in helping define the choice

of continuum shape and the gases to be included in the model. Figure 4 shows the integrated spectra within this aperture, along with the best-fitting PSG model gas emission components. For the 4.7 μ m region, we also tentatively identified an emission band at 4.85 μ m consistent with OCS, which was included in the fit. Additional details on the continuum fitting and spectral modeling procedure are given in Appendix B.

After modeling the nucleus-centered IFU extract, we proceeded to derive production rates and rotational temperatures as a function of ρ , by extracting and modeling the data within successive 0".625-wide annular sectors, as shown in the inset diagram of Figure 5. The resulting production rates as a function of ρ (referred to as "Q curves") are also shown in Figure 5

For the nucleus-centered extract (1.25-diameter circle), our best-fitting models give $Q(\text{CO}_2) = (9.50 \pm 0.05) \times 10^{26} \text{ s}^{-1}$, $Q(\text{CO}) = (1.70 \pm 0.04) \times 10^{26} \text{ s}^{-1}$ and $Q(\text{H}_2\text{O}) = (1.07 \pm 0.08) \times 10^{26} \text{ s}^{-1}$, and $Q(\text{OCS}) = (8.9 \pm 2.0) \times 10^{23} \text{ s}^{-1}$. From the Q-curve analysis, "terminal" gas production rates were derived for the annular sectors furthest from the nucleus. These provide an improved view of the coma mixing ratios, avoiding the optical depth effects that impact CO_2 in the nucleus-centered extract, although they could contain additional contributions from extended/distributed coma sources. The resulting (whole-coma equivalent) terminal gas production rates are $Q(\text{CO}_2) = (1.70 \pm 0.01) \times 10^{27} \text{ s}^{-1}$, $Q(\text{CO}) = (3.7 \pm 0.2) \times 10^{26} \text{ s}^{-1}$, $Q(\text{H}_2\text{O}) = (2.23 \pm 0.08) \times 10^{26} \text{ s}^{-1}$, and $Q(\text{OCS}) = (1.7 \pm 0.9) \times 10^{24} \text{ s}^{-1}$.

The Q curves for CO_2 and CO (Figure 5) level off towards larger nucleocentric distances, indicating that gas production for these species is confined within \sim 3000 km of the nucleus. On the other hand, the H_2O Qcurve shows no clear asymptote, and the error bars allow for the possibility of continued H₂O production towards the edge of the NIRSpec IFU. Therefore, we cannot rule out a contribution to H₂O gas in the outer coma from sublimating icy grains, which may be expected based on our detection of coma H_2O ice. Our terminal $Q(H_2O)$ value is significantly smaller than the value of (1.36 \pm $(0.35) \times 10^{27} \text{ s}^{-1}$ measured at $r_H = 2.9$ au by Z. Xing et al. (2025). This could be due to a rapid increase in H_2O production between $r_H = 3.3-2.9$ au, with a possible contribution from icy-grain sublimation within the relatively large, 20,000 km diameter Swift aperture.

Although $^{13}\text{CO}_2$ is securely detected in the nucleus-centered extract (Figure 4), optical depth effects and blending with the $^{12}\text{CO}_2$ wing preclude the derivation of a reliable $^{13}\text{CO}_2$ production rate in this region. We attempted to retrieve $Q(^{13}\text{CO}_2)$ in the annular sector between 0.65-1.65 from the nucleus, but only an upper

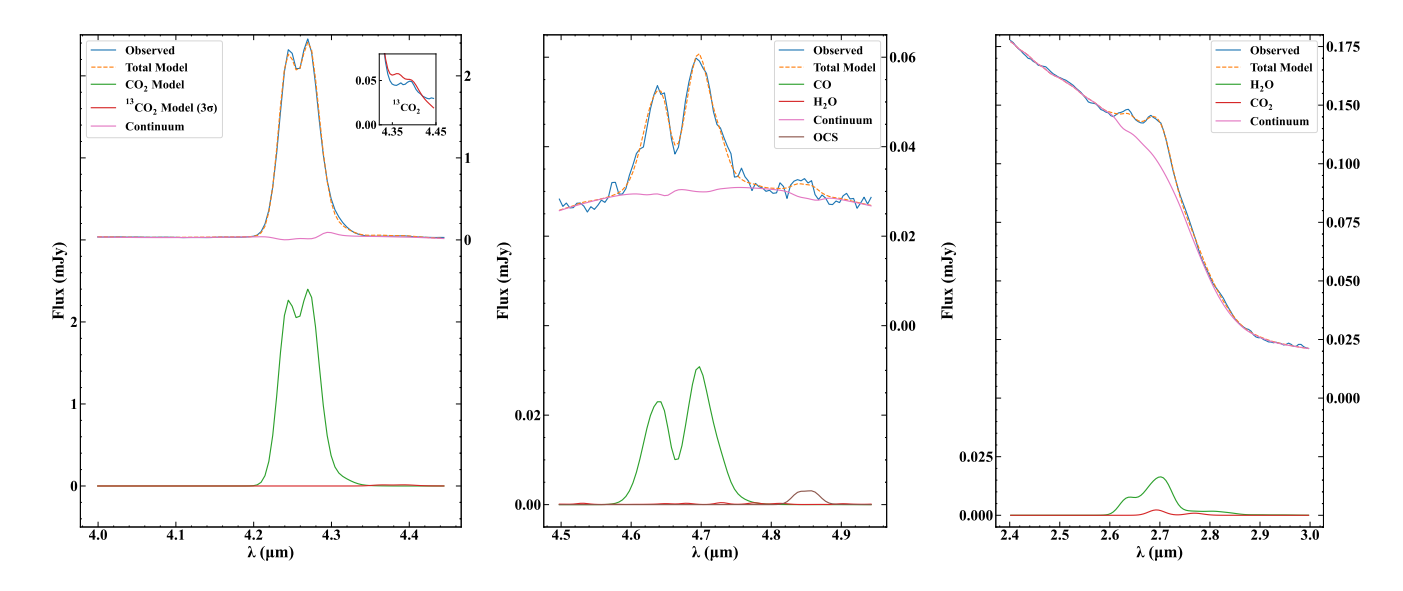


Figure 4. Observed NIRSpec molecular spectra of 3I/ATLAS extracted within a 0".625-radius circular aperture centered on the (pseudo-)nucleus, along with best-fitting gas and continuum models. The left ordinate axes apply to the model gas component fluxes (lower traces), whereas the right ordinates are for the observed spectrum, total model and continuum model components (upper traces). The weak 13 CO₂ band at 4.4 μ m is shown in the inset panel next to the main CO₂ band, with 3σ upper limit spectral model overlaid.

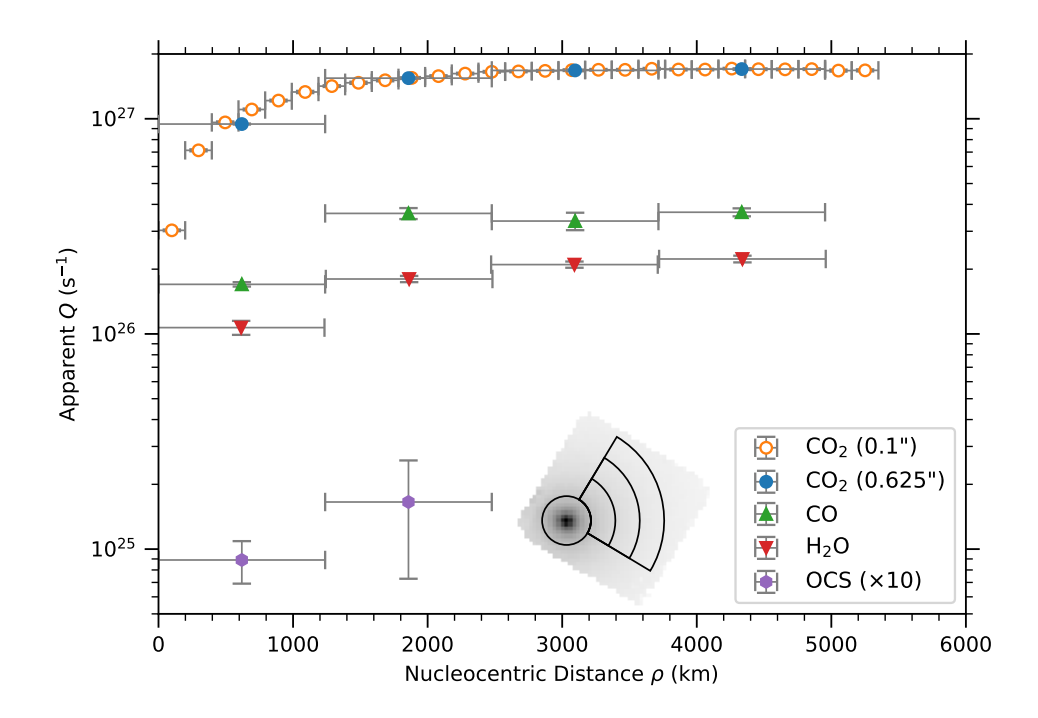


Figure 5. Best fitting production rates for CO_2 , CO, H_2O and OCS as a function of distance from the nucleus (Q curves). Spectra were extracted and modeled within four spatial regions of the IFU, as shown in the inset diagram, consisting of a central 0".625-radius circle, followed by three successive partial annular sectors, each with a 0".625 radial extent. Due to its higher SNR, CO_2 was also modeled within successive 0".1 annuli surrounding the nucleus. OCS values have been scaled up by a factor of 10 for display. Vertical error bars indicate 1σ statistical uncertainties, while the horizontal error bars indicate the radial extent of each spatial region.

limit $Q(^{13}\text{CO}_2) < 1.8 \times 10^{25} \text{ s}^{-1}$ could be obtained, resulting in a (3σ) lower limit on the $^{12}\text{C}/^{13}\text{C}$ ratio of > 63, which is formally consistent with the terrestrial value of 89 (T. B. Coplen et al. 2002). See Appendix B for further details.

5. DISCUSSION

Our JWST NIRSpec observations reveal that 3I/ATLAS contains a substantial volatile ice inventory, with a gas coma unusually rich in CO_2 relative to $\mathrm{H}_2\mathrm{O}$ and CO . In the absence of clear detections of other gases, it is reasonable to infer that CO_2 outgassing provides the dominant driving force for 3I's nucleus activity, and is responsible for launching dust grains away from the nucleus to produce the distinctive scattered light coma observed at $\sim 1.2~\mu\mathrm{m}$ and shorter wavelengths.

For previously-observed comets in our Solar System, the relative coma abundances of CO₂, CO, and H₂O are known to vary widely (up to several orders of magnitude) between different comets, with some of the variability attributed to the differing relative volatilities of these species as a function of temperature (T. Ootsubo et al. 2012; M. F. A'Hearn et al. 2012; O. Harrington Pinto et al. 2022). Indeed, variation in the coma CO₂/H₂O and CO/H₂O mixing ratios as a function of heliocentric distance is both theoretically predicted and observed (U. Marboeuf & B. Schmitt 2014; O. Harrington Pinto et al. 2022). However, compared with previous comets observed at similar heliocentric distances $(r_H \sim 3\text{--}4 \text{ au})$, the CO₂-dominated outgassing in 3I/ATLAS appears unusual. In Figure 6, we plot the CO₂/H₂O coma mixing ratio measured in previous comets as a function of r_H , and draw a log-linear trend line, fitted to the combined dataset of long- and shortperiod comets (excluding the peculiar outlier C/2016 R2 and the lower limit for C/2024 E1). The fit is weighted by the data uncertainties; where no uncertainties were available, an error bar of 10% was assumed.

The interstellar object 3I/ATLAS has a coma $\rm CO_2/H_2O$ ratio of 7.6 ± 0.3 , which is 18 times larger than expected for its heliocentric distance, based on the fit to previously observed cometary data (Figure 6). This corresponds to 4.5σ away from the trend line, and shows that 3I's coma $\rm CO_2/H_2O$ ratio is unusually high. The only other comet known to have a $\rm CO_2/H_2O$ ratio so far outside the normal Solar System trend is C/2016 R2 (PanSTARRS) (A. J. McKay et al. 2019). C/2016 R2 is considered to be one of the most peculiar comets ever observed, as a result of its large hypervolatile content (N. Biver et al. 2018; M. A. Cordiner et al. 2022) and correspondingly high CO/H₂O ratio. The CO/H₂O ratio of 1.65 ± 0.09 in 3I/ATLAS, on the other hand, is

more compatible with previous cometary observations, which have values < 7 between $r_H = 3$ –4 au (O. Harrington Pinto et al. 2022). Intriguingly, our CO/H₂O ratio is within the range of values (1.3–1.6) measured in 2I/Borisov at $r_H = 2.0$ au, although the H₂O production rate was observed to be falling rapidly around the time of those observations (D. Bodewits et al. 2020).

Due to the presence of water ice in cometary comae at $\gtrsim 3$ au (e.g. E. Lellouch et al. 1998; H. Kawakita et al. 2004; S. Protopapa et al. 2018), previous measurements of the gas $\mathrm{CO_2/H_2O}$ ratio using larger spectroscopic apertures (e.g. T. Ootsubo et al. 2012) could have been impacted by icy grain sublimation, thus reducing the observed ratio. It is difficult to assess the full impact this would have on the points around $r_H=3-4$ au in Figure 6, so further observations of 3I/ATLAS are recommended, closer to perihelion.

The active sublimating surface area for each of our detected gases is calculated in Appendix C. Following the analysis of D. Jewitt et al. (2025), the CO₂ active area of 3.1 km² is sufficient to drive the development of 3I's observed dust coma, even if the dust grains are relatively large ($\sim 100 \ \mu \mathrm{m}$) in size. The relatively small active area for H₂O (2.2 km²) could be partly explained by the relatively high sublimation temperature of H_2O (M. Womack et al. 2017), if the internal temperature of most of the nucleus (T_{nuc}) was in the range $T_{sub}(H_2O) > T_{nuc} > T_{sub}(CO_2)$ (but still close enough to $T_{sub}(H_2O)$ to allow some H_2O sublimation), at the time of our observations. Sublimation of H₂O may therefore become more fully activated as 3I/ATLAS moves closer to the Sun (T. H. Puzia et al. 2025), in which case a more accurate picture of the nucleus composition will be obtained. The very high CO₂/H₂O ratio observed by JWST could therefore indicate that T_{nuc} is lower than that experienced by typical Solar System comets at a similar r_H . This could arise as a result of a higher albedo or lower thermal conductivity of the nucleus surface layer compared with typical comets, leading to reduced heating or heat penetration. Higher albedo could be caused by a more ice-rich surface composition than normal, whereas lower thermal conductivity could arise from the presence of a volatile-depleted crust/mantle (A. Guilbert-Lepoutre et al. 2015). The latter was hypothesized for 1I/'Oumuamua, as a result of irradiation by cosmic rays during the object's interstellar passage (A. Fitzsimmons et al. 2018). Accounting for the lower volatility of H₂O using the (J. J. Cowan & M. F. A'Hearn 1979) ice sublimation model, we predict $CO_2/H_2O \sim 3.2$ at $r_H = 1$ au, which is still an order of magnitude larger than other comets observed near $r_H = 1$ au (Figure 6).

8 CORDINER ET AL.

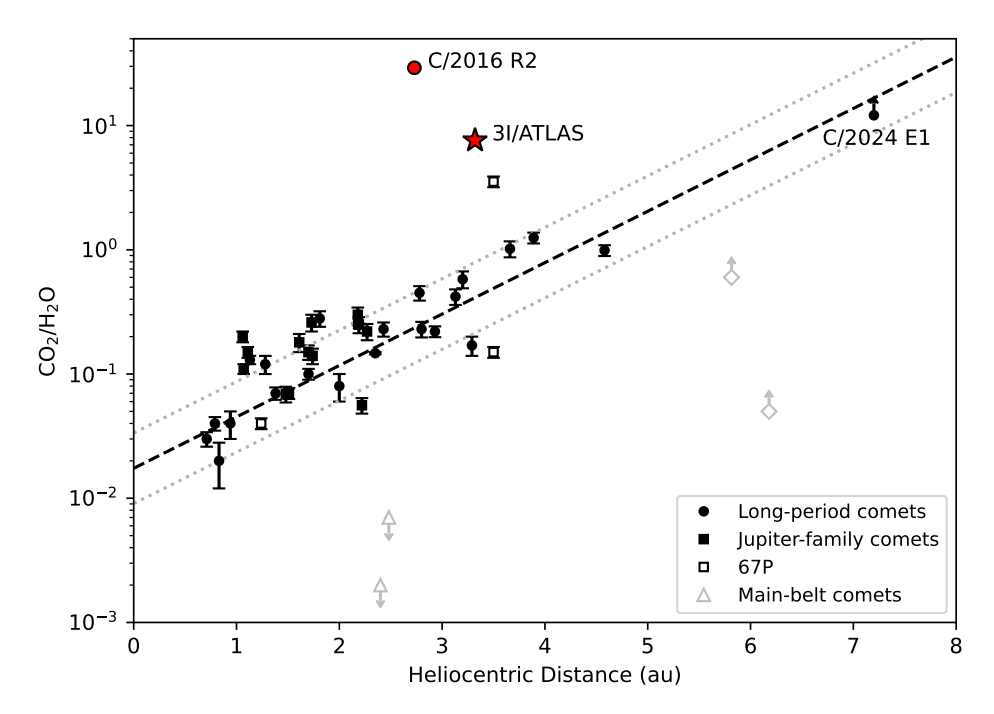


Figure 6. Coma CO_2/H_2O mixing ratios as a function of heliocentric distance for previously-observed comets, grouped by category: (1) long-period comets (LPCs), including Oort Cloud and Halley-type comets, (2) Jupiter-family comets (JFCs), (3) Main-belt comets (MBCs), and (4) Centaurs. Data are from the compilation of O. Harrington Pinto et al. (2022), with additional values from M. S. P. Kelley et al. (2023); O. Harrington Pinto et al. (2023); H. H. Hsieh et al. (2025); C. E. Woodward et al. (2025); C. Snodgrass et al. (2025). Values for 67P/Churyumov-Gerasimenko at $r_H = 3.5, 1.2, 3.5$ au (pre- to post-perihelion) are included, from M. Combi et al. (2020). Upper and lower limits are shown with arrows. A log-linear curve is fitted to the combined LPC + JFC dataset (dashed line), with $\pm 1\sigma$ margins shown as dotted grey lines (where σ is the standard deviation of the data from the fit). The peculiar, hypervolatile-rich comet C/2016 R2 was excluded from the fit. 3I/ATLAS (red star) is labeled, in addition to the lower limit for the recently-observed distant Oort cloud comet C/2024 E1 (C. Snodgrass et al. 2025).

CO₂/H₂O ratios greater than unity have been only rarely observed in previous comets. This is likely due to a combination of factors, including (1) relatively sparse number statistics due to the difficulty of observing comets beyond $r_H \gtrsim 3$ au (where H₂O sublimation is strongly suppressed), and (2) the difficulty of CO₂ observations in the pre-JWST era, due to telluric obscuration in the 4.3 μm region. Furthermore, bulk cometary CO₂/H₂O ice abundances are typically less than a few tens of percent (A. C. A. Boogert et al. 2015); a median coma CO₂/H₂O ratio of 17% was measured by T. Ootsubo et al. (2012), and a bulk, mission-integrated value of 7% was derived for comet 67P/Churyumov-Gerasimenko (M. Läuter et al. 2020). Indeed, considering the theory that a significant fraction of cometary ice originates in the interstellar medium (P. Ehrenfreund & S. B. Charnley 2000; M. N. Drozdovskaya et al. 2016), where CO_2/H_2O ratios are ~ 10 -50 % (A. C. A. Boogert et al. 2015; Z. L. Smith et al. 2025), a bulk CO₂/H₂O ratio in excess of unity for 3I/ATLAS would be surprising, perhaps hinting at an

unusual, carbon-rich chemical composition for this object.

CO₂ is thought to form during the interstellar and protoplanetary disk phases of star formation as a result of reactions between CO and OH on dust grain surfaces. The formation of CO₂ competes with the formation of H_2O from OH + H reactions (J. A. Noble et al. 2011). Under dark, non-irradiated conditions, the barrierless hydrogenation reaction resulting in H₂O dominates. However, upon exposure to UV radiation and cosmic rays, physicochemical models show that CO₂ may start to dominate the ice inventory (M. N. Drozdovskaya et al. 2016). S. Notsu et al. (2021) determined that CO₂ ice abundances are maximized at moderate $(10^{29} - 10^{30} \text{ erg s}^{-1}) \text{ X-ray luminosities in protostel-}$ lar envelopes. Various combinations of physicochemical evolutionary scenarios can theoretically produce zones with $CO_2/H_2O > 1$ in protoplanetary disks, for example: (1) beyond 30 au in the midplanes of larger, UVirradiated, infall-dominated disks (M. N. Drozdovskaya et al. 2016), (2) at a few au over longer timescales due to cosmic ray effects (C. Eistrup et al. 2018), or (3) in

elevated disk layers due to UV irradiation from the central protostar (K. Furuya et al. 2022). Furthermore, as shown by D. J. Stevenson & J. I. Lunine (1988), diffusion of sublimated gas outward across the ice line, where it subsequently freezes out, can result in significantly enhanced abundances of that ice. E. M. Price et al. (2021) modeled this effect for CO in the presence of inwarddrifting icy pebbles, to explain the high CO/H₂O ratio 2I/Borisov, so a similar enrichment of solid CO₂ may be expected in protoplanetary disks, just outside the CO_2 ice line. An intrinsically CO_2 -rich composition for a fraction of the interstellar object population, formed in such regions, may therefore result. Additional theoretical modeling will be required to determine whether a high CO₂/H₂O ratio could be compatible with an origin for 3I/ATLAS in the low metallicity, thick-disk Galactic stellar population, as suggested by M. J. Hopkins et al. (2025).

6. CONCLUSION

We performed JWST NIRSpec imaging spectroscopy of the interstellar object 3I/ATLAS at $r_H = 3.32$ au on the inbound leg of its flight through the Solar System. Rovibrational emission bands were detected of CO₂, CO and H₂O, in addition to dust and ice solid-state features, demonstrating the presence of a substantial, gasand ice-rich coma comparable to that of comets from our own Solar System. The CO₂ band at 4.3 μ m was particularly strong. The CO_2/H_2O mixing ratio of 7.6 ± 0.3 is 4.5σ above the trend as a function of r_H observed in long-period and Jupiter-family comets (excluding the peculiar C/2016 R2), and suggests the possibility of an intrinsically CO₂-rich nucleus. Such a high CO₂/H₂O ratio has never before been observed in a comet between $r_H = 3-4$ au. The combined capabilities of the JWST and Vera C. Rubin Legacy Survey of Space and Time (Ż. Ivezić et al. 2019) will facilitate additional observations of Solar System comets at such distances, to help improve the statistics and confirm whether 3I/ATLAS is as unusual as it appears.

A low coma H_2O abundance could also be implied by our data, possibly arising as a result of reduced heat penetration through an unusually thick, insulating crust or mantle. In that case, the sublimation of the less volatile H_2O ice could be inhibited relative to the (more volatile) CO_2 and CO ices. Further observations at distances $r_H < 3$ au will be needed, to facilitate measurement of the bulk nucleus composition of 3I/ATLAS as it passes closer to the Sun and the sublimation of H_2O (and other low-volatility ices) becomes more fully activated.

Software: George (S. Ambikasaran et al. 2015), JWST Calibration Pipeline software version v1.19.1

(H. Bushouse et al. 2025), Matplotlib (J. D. Hunter 2007), Numpy (C. R. Harris et al. 2020), Small-Bodies-Node/ice-sublimation (M. Van Selous & M. Kelley 2021), Planetary Spectrum Generator (PSG; G. L. Villanueva et al. 2018), sbpy (M. Mommert et al. 2019)

ACKNOWLEDGMENTS

This work is based on observations made with the NASA/ESA/CSA James Webb Space Telescope. The data were obtained from the Mikulski Archive for Space Telescopes at the Space Telescope Science Institute, which is operated by the Association of Universities for Research in Astronomy, Inc., under NASA contract NAS 5-03127 for JWST. Astrometric measurements of 3I/ATLAS were obtained using the ESO VLT FORS2 instrument at the La Silla Paranal Observatory, under program ID 115.29F8. We gratefully acknowledge the assistance of other optical observers who submitted astrometric observations of 3I/ATLAS in the weeks leading up to our observations, to help refine the ephemeris position — in particular, T. Lister, M. Banister, Q. Ye, and D. Seligman. John Stansberry is acknowledged for his assistance with scheduling the JWST observations. Supporting astrometric observations were obtained by the Comet Chasers school outreach program (https://www.cometchasers. org/), led by Helen Usher, which is funded by the UK Science and Technology Facilities Council (via the DeepSpace2DeepImpact Project), the Open University and Cardiff University. It accesses the LCOGT telescopes through the Schools Observatory/Faulkes Telescope Project (TSO2025A-00 DFET-The Schools' Observatory), which is partly funded by the Dill Faulkes Educational Trust, and through the LCO Global Sky Partners Programme (LCOEPO2023B-013). Observers included E. Maciulis, A. Bankole, J. Bowker, A. Trawiki, K. Golabek, L. Garrett, O. Roberts, T. Oladunjoye, participants on the British Astronomical Associations Work Experience project 2025, and representatives from the following schools and clubs: The Coopers Company & Coborn School; Upminster, UK; Ysgol Gyfun Gymraeg Bro Edern, Cardiff, UK; St Marys Catholic Primary School, Bridgend, UK; Institut d'Alcarràs, Catalonia, Spain; Louis Cruis Astronomy Club, Brazil; Srednja škola Jelkovec (Jelkovec High School), Zagreb, Croatia. D.F. conducted this research at the Jet Propulsion Laboratory, California Institute of Technology, under a contract with the National Aeronautics and Space Administration (80NM0018D0004). This research has made use of NASA's Astrophysics Data System Bibliographic Services. This research has made use of data

10 CORDINER ET AL.

and/or services provided by the International Astronomical Union's Minor Planet Center. M.E.S. acknowledge support in part from UK Science and Technology Facilities Council (STFC) grant ST/X001253/1.

Data Access Statement: All JWST data are available through the Mikulski Archive for Space Telescopes at the Space Telescope Science Institute under proposal ID #5094 (https://doi.org/10.17909/1jvn-1z72). The data products are under a three month embargo.

REFERENCES

- A'Hearn, M. F., Schleicher, D. G., Millis, R. L., Feldman,P. D., & Thompson, D. T. 1984, AJ, 89, 579,doi: 10.1086/113552
- A'Hearn, M. F., Feaga, L. M., Keller, H. U., et al. 2012, Astrophysical Journal, 758, 29, doi: 10.1088/0004-637x/758/1/29
- Alarcon, M. R., Serra-Ricart, M., Licandro, J., et al. 2025, The Astronomer's Telegram, 17264, 1
- Ambikasaran, S., Foreman-Mackey, D., Greengard, L., Hogg, D. W., & O'Neil, M. 2015, IEEE Transactions on Pattern Analysis and Machine Intelligence, 38, 252, doi: 10.1109/TPAMI.2015.2448083
- Biver, N., Bockelée-Morvan, D., Paubert, G., et al. 2018, A&A, 619, A127, doi: 10.1051/0004-6361/201833449
- Bodewits, D., Noonan, J. W., Feldman, P. D., et al. 2020, Nature Astronomy, 4, 867, doi: 10.1038/s41550-020-1095-2
- Bohlin, R. C., Gordon, K. D., & Tremblay, P. E. 2014, PASP, 126, 711, doi: 10.1086/677655
- Böker, T., Arribas, S., Lützgendorf, N., et al. 2022, A&A, 661, A82, doi: 10.1051/0004-6361/202142589
- Boogert, A. C. A., Gerakines, P. A., & Whittet, D. C. B. 2015, ARA&A, 53, 541,
 - doi: 10.1146/annurev-astro-082214-122348
- Bushouse, H., Eisenhamer, J., Dencheva, N., et al. 2025, JWST Calibration Pipeline, 1.19.1 Zenodo, doi: 10.5281/zenodo.16280965
- Chandler, C. O., Bernardinelli, P. H., Jurić, M., et al. 2025, arXiv e-prints, arXiv:2507.13409, doi: 10.48550/arXiv.2507.13409
- Combi, M., Shou, Y., Fougere, N., et al. 2020, Icarus, 335, 113421, doi: 10.1016/j.icarus.2019.113421
- Combi, M. R. 1994, AJ, 108, 304, doi: 10.1086/117070
- Coplen, T. B., Hopple, J. A., Böhlke, J. K., et al. 2002, Compilation of minimum and maximum isotope ratios of selected elements in naturally occurring terrestrial materials and reagents,, U.S. Geological Survey, Toxic Substances Hydrology Program, USGS Water-Resources Investigations Report, ix, 98 p. doi: 10.3133/wri014222
- Cordiner, M. A., Milam, S. N., Biver, N., et al. 2020, Nature Astronomy, 4, 861, doi: 10.1038/s41550-020-1087-2

- Cordiner, M. A., Coulson, I. M., Garcia-Berrios, E., et al. 2022, ApJ, 929, 38, doi: 10.3847/1538-4357/ac5893
- Cowan, J. J., & A'Hearn, M. F. 1979, Moon and Planets, 21, 155, doi: 10.1007/BF00897085
- Dones, L., Weissman, P. R., Levison, H. F., & Duncan, M. J. 2004, in Comets II, ed. M. C. Festou, H. U. Keller, & H. A. Weaver, 153
- Drozdovskaya, M. N., Walsh, C., van Dishoeck, E. F., et al. 2016, MNRAS, 462, 977, doi: 10.1093/mnras/stw1632
- Ehrenfreund, P., & Charnley, S. B. 2000, ARA&A, 38, 427, doi: 10.1146/annurev.astro.38.1.427
- Eistrup, C., Walsh, C., & van Dishoeck, E. F. 2018, A&A, 613, A14, doi: 10.1051/0004-6361/201731302
- Fitzsimmons, A., Snodgrass, C., Rozitis, B., et al. 2018, Nature Astronomy, 2, 133, doi: 10.1038/s41550-017-0361-4
- Foreman-Mackey, D., Hogg, D. W., Lang, D., & Goodman, J. 2013, PASP, 125, 306, doi: 10.1086/670067
- Furuya, K., Lee, S., & Nomura, H. 2022, ApJ, 938, 29, doi: 10.3847/1538-4357/ac9233
- Gardner, J. P., Mather, J. C., Abbott, R., et al. 2023, PASP, 135, 068001, doi: 10.1088/1538-3873/acd1b5
- Guilbert-Lepoutre, A., Besse, S., Mousis, O., et al. 2015, SSRv, 197, 271, doi: 10.1007/s11214-015-0148-9
- Guzik, P., & Drahus, M. 2021, Nature, 593, 375, doi: 10.1038/s41586-021-03485-4
- Harrington Pinto, O., Womack, M., Fernandez, Y., & Bauer, J. 2022, PSJ, 3, 247, doi: 10.3847/PSJ/ac960d
- Harrington Pinto, O., Kelley, M. S. P., Villanueva, G. L., et al. 2023, PSJ, 4, 208, doi: 10.3847/PSJ/acf928
- Harris, C. R., Millman, K. J., van der Walt, S. J., et al. 2020, Nature, 585, 357, doi: 10.1038/s41586-020-2649-2
- Hopkins, M. J., Dorsey, R. C., Forbes, J. C., et al. 2025, ApJL, 990, L30, doi: 10.3847/2041-8213/adfbf4
- Hsieh, H. H., Noonan, J. W., Kelley, M. S. P., et al. 2025, PSJ, 6, 3, doi: 10.3847/PSJ/ad9199
- Huebner, W. F., & Mukherjee, J. 2015, Planet. Space Sci., 106, 11, doi: 10.1016/j.pss.2014.11.022
- Hunter, J. D. 2007, Computing in Science & Engineering, 9, 90, doi: 10.1109/MCSE.2007.55
- Ivezić, Ž., Kahn, S. M., Tyson, J. A., et al. 2019, ApJ, 873, 111, doi: 10.3847/1538-4357/ab042c

- Jewitt, D., Hui, M.-T., Mutchler, M., Kim, Y., & Agarwal, J. 2025, ApJL, 990, L2, doi: 10.3847/2041-8213/adf8d8
- Jewitt, D., & Luu, J. 2025, The Astronomer's Telegram, 17263, 1
- Jones, T. J., Stark, D., Woodward, C. E., et al. 2008, AJ, 135, 1318, doi: 10.1088/0004-6256/135/4/1318
- Kareta, T., Champagne, C., McClure, L., et al. in press, ApJL, arXiv:2507.12234, doi: 10.48550/arXiv.2507.12234
- Kawakita, H., Watanabe, J.-i., Ootsubo, T., et al. 2004, ApJL, 601, L191, doi: 10.1086/382073
- Kelley, M. S. P., Hsieh, H. H., Bodewits, D., et al. 2023, Nature, 619, 720, doi: 10.1038/s41586-023-06152-y
- Läuter, M., Kramer, T., Rubin, M., & Altwegg, K. 2020, MNRAS, 498, 3995, doi: 10.1093/mnras/staa2643
- Lellouch, E., Crovisier, J., Lim, T., et al. 1998, A&A, 339, L9
- Leto, G., & Baratta, G. A. 2003, A&A, 397, 7, doi: 10.1051/0004-6361:20021473
- Levison, H. F., Duncan, M. J., Brasser, R., & Kaufmann,D. E. 2010, Science, 329, 187,doi: 10.1126/science.1187535
- Marboeuf, U., & Schmitt, B. 2014, Icarus, 242, 225, doi: 10.1016/j.icarus.2014.07.001
- Mastrapa, R. M., Sandford, S. A., Roush, T. L., Cruikshank, D. P., & Dalle Ore, C. M. 2009, ApJ, 701, 1347, doi: 10.1088/0004-637X/701/2/1347
- McKay, A. J., DiSanti, M. A., Kelley, M. S. P., et al. 2019, AJ, 158, 128, doi: 10.3847/1538-3881/ab32e4
- Minev, M., Kostov, A., & Mutafov, A. 2025, The Astronomer's Telegram, 17275, 1
- Mommert, M., Kelley, M., de Val-Borro, M., et al. 2019, The Journal of Open Source Software, 4, 1426, doi: 10.21105/joss.01426
- Moore, M. H., & Hudson, R. L. 1992, ApJ, 401, 353, doi: 10.1086/172065
- Noble, J. A., Dulieu, F., Congiu, E., & Fraser, H. J. 2011, ApJ, 735, 121, doi: 10.1088/0004-637X/735/2/121
- Notsu, S., van Dishoeck, E. F., Walsh, C., Bosman, A. D., & Nomura, H. 2021, A&A, 650, A180, doi: 10.1051/0004-6361/202140667
- Ootsubo, T., Kawakita, H., Hamada, S., et al. 2012, ApJ, 752, 15, doi: 10.1088/0004-637X/752/1/15
- Opitom, C., Jehin, E., Hutsemékers, D., et al. 2021, A&A, 650, L19, doi: 10.1051/0004-6361/202141245
- 'Oumuamua ISSI Team, Bannister, M. T., Bhandare, A., et al. 2019, Nature Astronomy, 3, 594, doi: 10.1038/s41550-019-0816-x

- Pfalzner, S., & Vincke, K. 2020, ApJ, 897, 60, doi: 10.3847/1538-4357/ab9533
- Price, E. M., Cleeves, L. I., Bodewits, D., & Öberg, K. I. 2021, ApJ, 913, 9, doi: 10.3847/1538-4357/abf041
- Protopapa, S., Kelley, M. S. P., Yang, B., et al. 2018, ApJL, 862, L16, doi: 10.3847/2041-8213/aad33b
- Protopapa, S., Sunshine, J. M., Feaga, L. M., et al. 2014, Icarus, 238, 191, doi: 10.1016/j.icarus.2014.04.008
- Puzia, T. H., Rahatgaonkar, R., Carvajal, J. P., Nayak,
 P. K., & Luco, B. 2025, ApJL, 990, L27,
 doi: 10.3847/2041-8213/adfa0b
- Raymond, S. N., Armitage, P. J., Veras, D., Quintana,
 E. V., & Barclay, T. 2018, MNRAS, 476, 3031,
 doi: 10.1093/mnras/sty468
- Seligman, D. Z., Micheli, M., Farnocchia, D., et al. 2025, ApJL, 989, L36, doi: 10.3847/2041-8213/adf49a
- Smith, Z. L., Dickinson, H. J., Fraser, H. J., et al. 2025,Nature Astronomy, 9, 883,doi: 10.1038/s41550-025-02511-z
- Snodgrass, C., Holt, C. E., Kelley, M. S. P., et al. 2025, MNRAS, 541, L8, doi: 10.1093/mnrasl/slaf046
- Stevenson, D. J., & Lunine, J. I. 1988, Icarus, 75, 146, doi: 10.1016/0019-1035(88)90133-9
- Taylor, A. G., & Seligman, D. Z. 2025, ApJL, 990, L14, doi: 10.3847/2041-8213/adfa28
- Tonry, J. L., Denneau, L., Heinze, A. N., et al. 2018, PASP, 130, 064505, doi: 10.1088/1538-3873/aabadf
- Van Selous, M., & Kelley, M. 2021, Github, commit:e20745b
- Villanueva, G., Liuzzi, G., Faggi, S., et al. 2025, in Fundamentals of the Planetary Spectrum Generator 2025 Edition, Vol. 1, 43–63
- Villanueva, G. L., Smith, M. D., Protopapa, S., Faggi, S., & Mandell, A. M. 2018, JQSRT, 217, 86, doi: 10.1016/j.jqsrt.2018.05.023
- Womack, M., Sarid, G., & Wierzchos, K. 2017, PASP, 129, 031001, doi: 10.1088/1538-3873/129/973/031001
- Woodward, C. E., Bockélee-Morvan, D., Harker, D. E., et al. 2025, PSJ, 6, 139, doi: 10.3847/PSJ/add1d5
- Xing, Z., Bodewits, D., Noonan, J., & Bannister, M. T. 2020, The Astrophysical Journal Letters, 893, L48, doi: 10.3847/2041-8213/ab86be
- Xing, Z., Oset, S., Noonan, J., & Bodewits, D. 2025, arXiv e-prints, arXiv:2508.04675, doi: 10.48550/arXiv.2508.04675
- Yang, B., Meech, K. J., Connelley, M., & Keane, J. V. 2025, arXiv e-prints, arXiv:2507.14916, doi: 10.48550/arXiv.2507.14916
- Zheng, X.-L., & Zhou, J.-L. 2025, MNRAS, 537, 3123, doi: 10.1093/mnras/staf234

12 CORDINER ET AL.

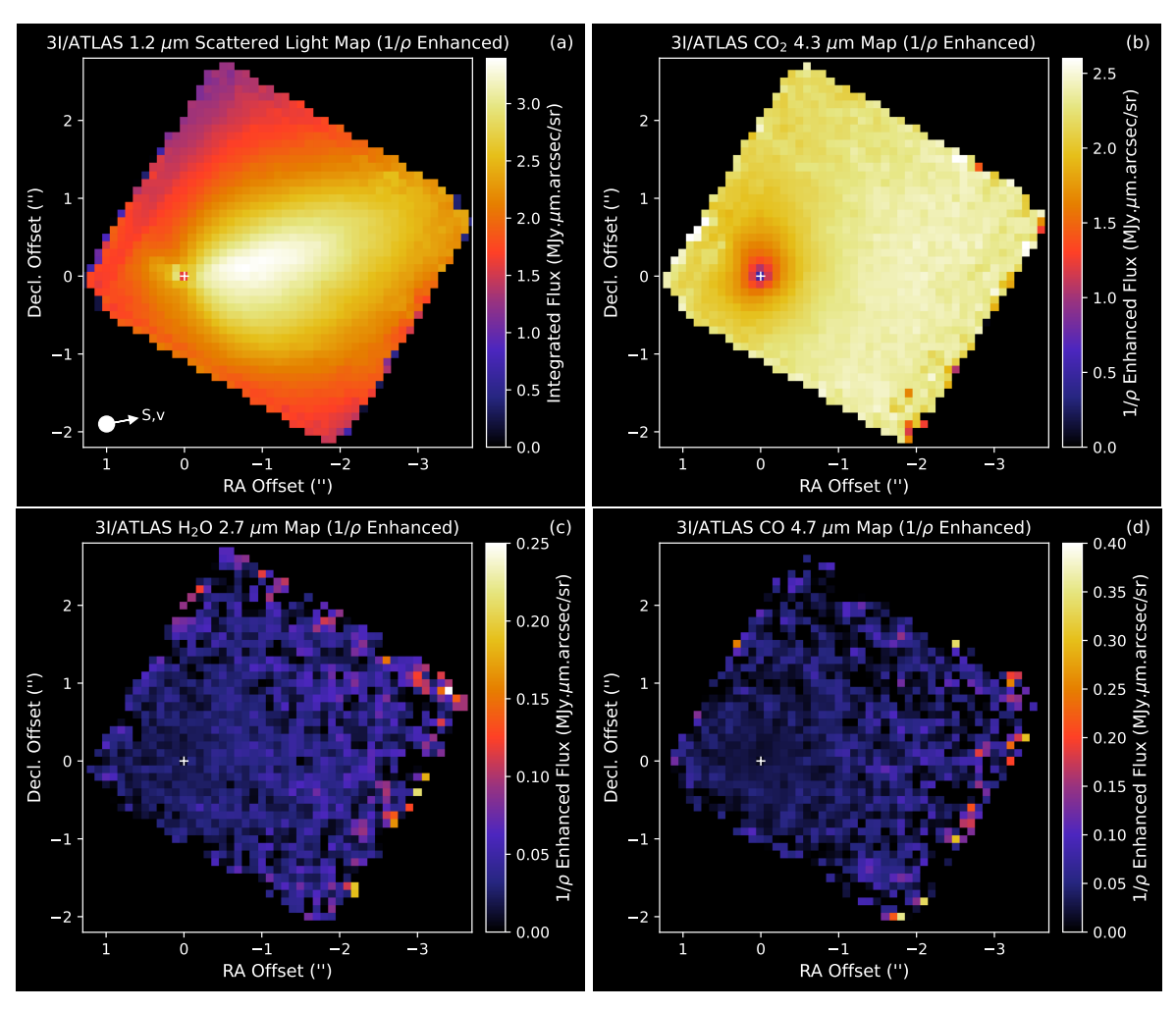


Figure 7. $1/\rho$ -enhanced flux maps for 3I/ATLAS observed using JWST NIRSpec. These are the images from Figure 2, multiplied by ρ (the sky-projected distance from the center of the brightest pixel), for (a) scattered light at 1.2 μ m, (b) CO₂ at 4.3 μ m, (c) H₂O at 2.7 μ m, and (d) CO at 4.7 μ m. Image axes are aligned with the equatorial (RA/decl.) grid. Panel (a) lower left corner shows the direction of the (sky-projected) comet-sun (S) and nucleus velocity (v) vectors (which are too close to distinguish). The white cross shows the position of the nucleus pixel.

APPENDIX

A. RADIALLY-ENHANCED FLUX MAPS

Figure 7 shows " $1/\rho$ enhanced" versions of the flux maps in Figure 2, where the dilution of the observed column density due to quasi-spherical expansion of the coma (which is proportional to $1/\rho$, where ρ is the sky-projected distance from the center of the nucleus pixel), has been divided out. The average value of ρ was calculated within each pixel using a 10×10 -point cartesian sub-sampling.

B. SPECTRAL MODELING

Gas production rates (Q) and rotational temperatures (T_{rot}) , were derived as a function of distance from the nucleus for CO₂, CO, and H₂O, using optimal estimation routines as part of the Planetary Spectrum Generator (PSG; G. L. Villanueva et al. 2018, based on synthetic fluorescence models described by G. Villanueva et al. 2025). We performed baseline fitting to subtract the (nucleus + dust) continuum based on fits to the spectral regions immediately adjacent to the lines of interest (Figure 4), adopting the conservative strategy of obtaining an good fit within the noise, using

a minimum number of free parameters. A 3rd-order polynomial was found to be sufficient for describing the continua underneath and surrounding the CO₂ and CO features, whereas for H₂O, we tried various analytic functions to produce a good fit, including the wing of the 3 μ m ice band. Although a 5th order polynomial was found to be sufficient to reproduce the shape of the continuum in this region, a lack of formal constraints across the 2.6–2.8 μ m region spanning the H₂O 2.7 μ m band led to increased uncertainties on $Q(\text{H}_2\text{O})$. Therefore, for H₂O, we adopted a more physically constrained continuum model, formed as the product of a linear slope and a sigmoid function:

$$R(\lambda) = (m(\lambda - \lambda_c) + b) \left(1 - \frac{L}{1 + e^{-\tau(\lambda - \lambda_b)}} \right),$$
(B1)

where $\lambda_c = 2.5 \ \mu\text{m}$ is the linear continuum normalization point, m is the linear slope, b is the y-intercept point, L is the depth of the 3- μ m band, τ controls the slope of the band edge, and λ_b controls the wavelength of the band edge. The (variable) exponential onset of the sigmoid function effectively matches the quasi-Gaussian shape of the blue wing of the 3 μ m H₂O ice band (G. Leto & G. A. Baratta 2003). By simultaneously optimizing the continuum and spectral line models, uncertainties in the fitted continuum shapes were included in the uncertainties derived for our best-fitting production rates. After experimenting with alternative functional forms for the continuum in the vicinity of our observed spectral lines, we found that the derived production rates remained consistent, within the errors.

The CO₂ and CO spectral regions were modeled using the methods described by C. E. Woodward et al. (2025). The gas outflow velocity was set at $0.44~\rm km\,s^{-1}$, based on the standard relationship $v=0.8r_H^{-0.5}$ (e.g. T. Ootsubo et al. 2012). Molecular photolysis rates appropriate for the active Sun were incorporated from W. F. Huebner & J. Mukherjee (2015). Pixels close to the nucleus can be affected by significant line opacity and PSF-related flux losses, which are difficult to accurately model. Therefore, after modeling the average spectrum within the $\rho=0.0.000$ nucleus-centered aperture, we proceeded with a "Q-curve" analysis, deriving the production rates and rotational temperatures as a function of ρ within successive (independent) partial annular sectors centered on the brightest (nucleus-containing) pixel. To avoid flux losses from pixels at the very edge of the IFU, and to focus on a uniform coma angular region, a 90° inscribed angle was used for all partial annuli, with radial bounds parallel to the north-east and south-east edges of the IFU; see inset diagram in Figure 5. We found a 0.0000 flux losses from the very high SNR for CO₂, we also generated a higher-resolution Q curve for this species using a 0.00000 annulus width. The resulting production rates and rotational temperatures as a function of ρ are shown in Figure 5.

For the 2.7 μ m region, H₂O spectral models were generated using PSG, while the continuum was determined using Equation B1, combined with the $\lambda/\Delta\lambda$ =5000 Solar spectral model of R. C. Bohlin et al. (2014). Additional (weak) spectral contributions from coma CO₂ to this region were added based on our best fit to the 4.3 μ m band. The H₂O production rate and rotational temperature were retrieved using a Gaussian processes approach within the George software package (S. Ambikasaran et al. 2015), and uncertainties were derived using a Markov Chain Monte Carlo algorithm (emcee; D. Foreman-Mackey et al. 2013). The retrieved rotational temperatures as a function of nucleocentric distance for each observed species are shown in Figure 8.

Examination of Figure 1 indicates the presence of $^{13}\text{CO}_2$ alongside $^{12}\text{CO}_2$, affording the first opportunity to test the $^{12}\text{CO}_2/^{13}\text{CO}_2$ ratio in an interstellar object. Compared to the much stronger $^{12}\text{CO}_2$ emission, the $^{13}\text{CO}_2$ band is only clearly detected in the the 0".625 nucleus-centered aperture. Unfortunately, the $^{12}\text{CO}_2$ in this region suffers from optical depth effects, and the low $(\lambda/\Delta\lambda\sim200)$ spectral resolution introduces additional difficulties in disentangling the contributions from each isotopologue. We therefore focused on analyzing the spectra from the first annular sector, where optical depth effects are reduced. We used the PSG to retrieve production rates $Q(^{12}\text{CO}_2) = (1.15\pm0.01)\times10^{27} \text{ s}^{-1}$ and $Q(^{13}\text{CO}_2) < 1.50\times10^{25} \text{ s}^{-1}$. This corresponds to a $^{12}\text{C}/^{13}\text{C}$ lower limit of $> 63~(3\sigma)$, which is formally consistent with the terrestrial value of 89. Additional observations of $^{13}\text{CO}_2$ in 3I/ATLAS at higher spectral resolution and signal-to-noise will be invaluable in separating it from its optically thick $^{12}\text{CO}_2$ counterpart, in order to place improved constraints on the CO₂ isotopic ratio.

C. ACTIVE SUBLIMATING SURFACE AREAS

We used the cometary ice thermal sublimation model of J. J. Cowan & M. F. A'Hearn (1979) to calculate the CO_2 , H_2O , and CO active surface areas, assuming an infrared emissivity of 0.95, albedo of 5% and nucleus radius of < 2.8 km (D. Jewitt et al. 2025). The Small-Bodies-Node/ice-sublimation code (M. Van Selous & M. Kelley 2021) was used to calculate the average sublimation rate per unit area, Z, at $r_H = 3.32$ au, assuming a non-rotating, spherical nucleus. The active area is derived by dividing our terminal Q values by Z, resulting in values of 3.1 km² for CO_2 , 2.2 km² for

14 Cordiner et al.

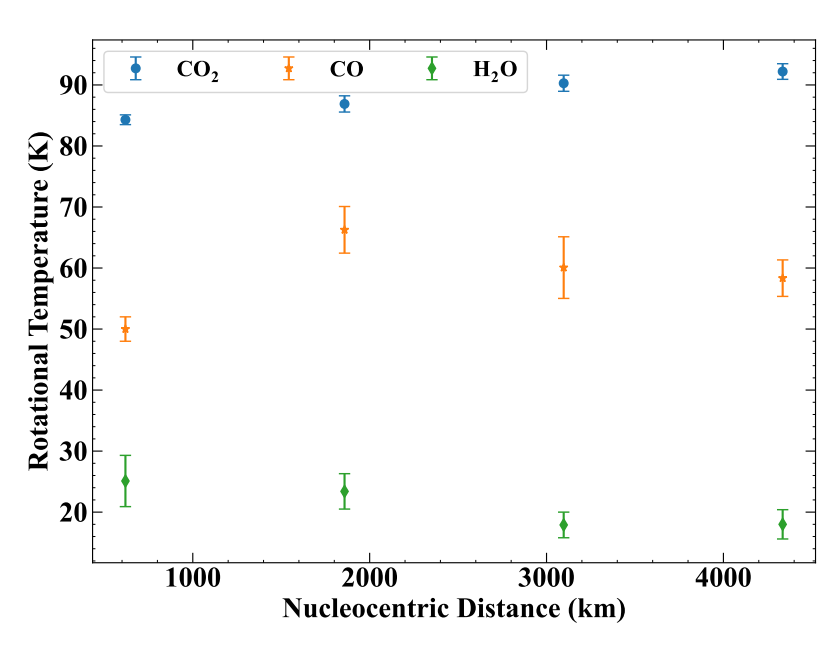


Figure 8. Best fitting rotational temperatures for CO₂, CO, and H₂O as a function of sky-projected distance from the nucleus.

 $\rm H_2O$, and 0.2 km² for CO. The active fractional area of the nucleus for each species is found by dividing these active areas by the (assumed) nucleus surface area. The corresponding lower limits on the active fractional area for each ice are > 3.1%, > 2.2%, and > 0.2%, respectively.